PNAS RESEARCH ARTICLE | CHEMISTRY

Energy landscape statistics and thermodynamics of a machine-learned model of water

Ryan J. Szukalo[a], Andreas Neophytou[b], Axel Gomez[a], Nicolas Giovambattista[c,d], Francesco Sciortino[b], and Pablo G. Debenedetti[e,1]

Affiliations are included on p. 8.

Contributed by Pablo G. Debenedetti; received November 25, 2025; accepted February 19, 2026; reviewed by Christoph Dellago and Andreas Heuer

Water's anomalous thermodynamic behavior arises from the presence of intricate hydrogen-bond networks that are highly sensitive to many-body interactions, challenging molecular modeling for decades. The ongoing machine learning revolution has opened the possibility of performing quantum-accurate liquid-structure calculations at affordable computational cost. Beyond reproducing water's thermodynamic properties with high fidelity, such simulations provide a stringent benchmark for theoretical models and a route to deeper physical understanding. We use the recently developed machine-learned Deep Potential Many-Body Polarizable water model to show that the free energy of supercooled water can be accurately modeled with the potential energy landscape formalism. The resulting equation of state predicts the presence of a liquid–liquid critical point in excellent agreement with recent estimates. Together with previous studies based on empirical classical water potentials, it confirms that the potential energy landscape of water is Gaussian, providing a unifying framework for extracting thermodynamic behavior across model complexity, from empirical force fields to quantum-trained neural network models.

supercooled water | machine-learned potentials | potential energy landscape | statistical mechanics

Water's distinctive physical and chemical behavior, from its density maximum at 4 °C to its anomalous properties in the supercooled regime, has long attracted the interest of scientists (1–6). These anomalies arise from water's capacity to form transient and directional hydrogen-bonds (7, 8). Linking local molecular structure to macroscopic thermodynamic responses remains a fundamental challenge in condensed matter physics and chemistry, with wide-ranging implications for climate modeling, cryobiology, and biological processes.

For over five decades, molecular simulations have provided the primary means for probing water at the microscopic level (9–12). Rigid, nonpolarizable empirical models, such as the simple point charge (SPC) and transferable interatomic potentials with n points (TIPnP), became workhorses for molecular simulation, reproducing many structural and thermodynamic properties despite neglecting explicit many-body interactions and polarization (10, 13, 14). These models achieved remarkable success, qualitatively capturing water's thermodynamic anomalies and phase diagram (15) and even suggesting the existence of a second critical point in the supercooled regime (2, 16). To impose a more realistic representation of the underlying physics, polarizable models [e.g., Thole-Type Model (TTM); Atomic Multipole Oriented Electrostatics and Bond Angles model (AMOEBA)] incorporate induction effects and thus provide a more physically grounded alternative to rigid force fields. Nonetheless, they remain constrained by analytical functional forms and empirical parameter fitting, which hinders systematic improvement and limits their transferability across thermodynamic states (17–20). These limitations highlight the need for a fundamentally different approach. Ab initio molecular dynamics (21) addresses this challenge by deriving forces directly from electronic structure theory, eliminating reliance on empirical parameterization. While computational cost still restricts accessible system sizes and time scales, the first-principles formulation establishes it as the most promising path toward a quantitatively reliable description of water across thermodynamic conditions (22–24).

The emergence of machine learning has transformed molecular modeling (25–27). Machine-learned potentials (MLPs) now routinely reproduce high-level quantum mechanical forces at a fraction of the cost, enabling simulations previously beyond reach (28). Researchers have developed several MLPs specifically for water (29–34). Many of these models, trained on density functional theory (DFT) data have successfully captured

Significance

Water's anomalous properties emerge from its complex hydrogen-bond networks in the liquid phase, which are difficult to model accurately. Quantum-level accuracy typically entails prohibitive computational costs, limiting large-scale simulations of liquid water. This work demonstrates that machine-learned potentials trained on quantum-mechanical calculations preserve the distinctive thermodynamics governing water's behavior while enabling large-scale simulations. By applying potential energy landscape theory to a machine-learned potential, we show that Gaussian landscape statistics persist across model complexity. This robustness validates the powerful combination of machine-learned potentials and energy landscape theory for studying the low-temperature behavior of complex materials.

Author contributions: R.J.S., N.G., F.S., and P.G.D. designed the research; R.J.S., A.N., A.G., and F.S. performed the research; and all authors analyzed the data and wrote the paper.

Reviewers: C.D., Universitat Wien; and A.H., Univ. of Muenster.

The authors declare no competing interest.

[1]To whom correspondence may be addressed. Email: pdebene@princeton.edu.

This article contains supporting information online at https://www.pnas.org/lookup/suppl/doi:10.1073/pnas.2534303123/-/DCSupplemental.

Published March 26, 2026.

the equilibrium phase diagram and liquid–liquid phase transition (35, 36), while other approaches have focused on reproducing specific thermodynamic properties (37, 38).

Recently, Bore and Paesani (39) leveraged the Deep Potential (DP) framework (40, 41) and developed an MLP (designated DP_MBpol) trained directly on MB-pol reference data rather than DFT calculations. MB-pol itself is a sophisticated, many-body polarizable force field derived from a rigorous many-body expansion of the energy and parameterized against coupled-cluster CCSD(T) calculations (42–44). Unlike empirical or polarizable force fields, which fit limited observables, MB-pol achieves systematic, quantum-chemistry–level accuracy from isolated clusters to bulk ice and liquid water (45, 46). It quantitatively captures hydrogen-bonding, vibrational spectra, and many structural and dynamical anomalies of water without empirical fitting to condensed-phase data.

However, MB-pol's computational cost, which arises from explicit many-body terms and self-consistent polarization calculations, limits accessible system sizes and simulation timescales. This limitation is addressed by the DP model, DP_MBpol, trained on over 50,000 configurations generated from MB-pol molecular dynamics simulations of liquid water and ice polymorphs spanning temperatures from 100 to 400 K and pressures up to 100 kbar (39). The resulting potential faithfully reproduces MB-pol energetics while providing approximately 20-fold improved computational efficiency relative to classical MD with MB-pol itself. Researchers have subsequently used this model to recover the experimental phase diagram of water (both liquid and crystal phases) below 1 GPa (39), to demonstrate the presence of a liquid-liquid critical point (47), and to investigate water's supercooled and glassy phenomenology (48).

Despite extensive work establishing the accuracy of MB-pol and DP_MBpol in reproducing water's structural, thermodynamic, and phase behavior (39, 42–44, 48), much less is known about their underlying energy landscape. In particular, the statistical organization of configurations, the manner in which accessible states evolve with density, and the relation between microscopic interactions and macroscopic anomalies remain largely unexplored.

The potential energy landscape (PEL) formalism provides a rigorous framework for connecting the statistical properties of the potential energy surface to the system free energy (49–54). In the PEL approach, configuration space is partitioned into basins and the partition function is written as a sum over all distinct basins. Each basin has an associated potential energy minimum, called an inherent structure (IS), and associated local curvature around its IS. An IS represents a mechanically stable configuration where all forces vanish. At finite temperature, the system vibrates within one basin and occasionally transitions between them, with the frequency of transitions decreasing as temperature decreases (50). Partitioning the PEL into basins results in a simple expression for the free energy, composed of only two contributions: the free energy of the system constrained to a typical basin (among those sampled at the specified temperature T and volume V) and an entropic term counting the number of available basins (again at the specified T and V). Researchers have applied the PEL approach to several empirical models of water (55–58), which all suggest that the number of basins with a prescribed IS energy is well described by a Gaussian distribution. This finding has opened the possibility of linking water's anomalies to the volume-dependence of the statistical properties of the PEL (56). Recent studies of flexible water models confirm that molecular flexibility alters but does not erase the core topological features underlying anomalous behavior (59). Extensions to include nuclear quantum effects (60–63) have refined the landscape perspective to include more detailed physics.

All prior PEL studies of water have relied on empirical or semiempirical force fields; specifically, SPC/E (55), TIP4P/2005 (57, 58), q-TIP4P/F (59), and ML-BOP (64). In all cases, the equation of state (EoS) derived from the PEL formalism is in remarkably good agreement with the corresponding molecular dynamics simulations. However, it remains unclear whether the features in the PEL of empirical water models persist for water models based on quantum mechanical calculations, such as MB-pol, where many-body interactions are included. We tackle this issue here by employing the DP_MBpol water model (39) to map water's PEL at densities from 0.92 to 1.27 g/cm^3. We demonstrate that the Gaussian landscape approximation holds at this level of accuracy and that PEL signatures of the density anomaly persist under the many-body interactions encoded by the Deep Potential model. Importantly, we quantify the statistical properties of the PEL in a system where a neural network implicitly specifies the underlying Hamiltonian rather than this being done through an empirical analytic form. That the expected landscape features emerge despite this fundamental change underscores both the robustness of the PEL framework (and in particular the Gaussian description) and the reliability of MLPs. Our results reveal that the nonmonotonic volume-dependence of IS energies and the systematic variation of basin shape are features central to water's anomalies, which persist in the MLP-based modeling. This work validates the generality of PEL principles across water models, from pair potentials to many-body neural networks, and establishes the PEL formalism as a powerful tool for interrogating the low-temperature behavior of complex, machine-learned Hamiltonians.

Results

Molecular Dynamics Simulations. To investigate the PEL of the DP_MBpol water model, we performed extensive equilibrium DPMD simulations of $N = 500$ molecules across a wide range of thermodynamic conditions. The system size of $N = 500$ molecules is comparable with or larger than previous PEL studies of water using classical force fields (55, 57, 59, 64). Fig. 1 presents a complete map of these simulations. The main set of state points (*Inset*, dark blue circles) forms a matrix spanning temperatures from 200 to 300 K and densities from 0.92 to 1.27 g/cm^3, chosen to encompass water's anomalous regime including the density maximum and be in close proximity to the DP_MBpol liquid–liquid critical region (47). From these state points, we extract the PEL parameters that govern water's thermodynamic behavior. The additional simulations shown in the broader diagram (yellow and red squares) summarize the thermodynamic integration (TI) pathways used to calculate absolute free energies. We discuss this TI scheme, which connects the liquid state points to an ideal gas reference via carefully chosen paths, in *SI Appendix*, section 3.

To generate ISs, we employ conjugate gradient minimization to quench equilibrium configurations obtained from NVT MD simulations at each state point to their nearest local minimum. We repeated this procedure for 100 independent configurations per state point, providing a statistically robust estimate of the mean inherent structure energy, E_{IS}, and its fluctuations. The quenching removes thermal fluctuations, revealing the underlying potential energy minima that serve as the skeleton of the potential energy landscape (49).

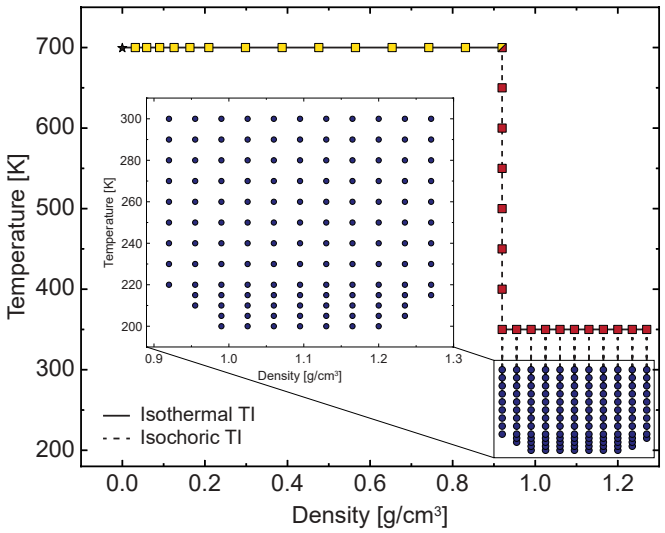

Fig. 1. State point diagram summarizing all molecular dynamics simulations performed in this study. The main simulation grid is shown as dark blue circles, covering temperatures from 200 to 300 K and densities from 0.92 to 1.27 g/cm^3 in order to probe water's anomalous regime, including both the density maximum and the proposed liquid–liquid critical region. Simulations used for thermodynamic integration (TI) are shown as yellow and red squares. Three TI paths are included: i) an isothermal path at $T = 700$ K that connects an ideal-gas reference state to a condensed phase while spanning densities from 0.006 to 0.92 g/cm^3, ii) an isochoric path at $\rho = 0.92$ g/cm^3 that cools the system from $T = 700$ K to 350 K and links the reference states to the main simulation points. iii) an isothermal path at $T = 350$ K from 0.92 to 1.27 g/cm^3, connecting to each density studied. Solid horizontal lines denote isothermal integration, while dashed vertical lines denote isochoric integration. The black star marks the ideal-gas reference point. Yellow squares correspond to simulations using the MB-pol potential, while all remaining points (red and blue) were simulated with the DP_MBpol model. The dual-colored square at $\rho = 0.92$ g/cm^3 and $T = 700$ K indicates the state where we converted the MB-pol free energy to DP_MBpol using a weighted ensemble overlap approach (*SI Appendix*, section 3). Together, these TI paths provide absolute free energies for all main state points relative to the ideal-gas reference. The *Inset* highlights the main simulation grid in greater detail.

Potential Energy Landscape Formalism. To describe the statistical properties of the PEL, we adopt the Gaussian approximation, which has proven effective for both Lennard-Jones-type model systems and water (55, 57, 64, 65). For a system of N water molecules with $n = 3N$ total atoms, the potential energy landscape is described by the hypersurface $V(\mathbf{r}^d)$ in $(d+1)$-dimensional space, where $d = 3n = 9N$ represents the total number of degrees of freedom. While DP_MBpol treats water as a collection of individual atoms rather than formal molecules (i.e., covalent bonds are not explicitly considered), the three-atom structure of water still emerges. In the Gaussian approximation of the PEL formalism, the number of basins with IS energy between e_{IS} and $e_{\mathrm{IS}} + \mathrm{d}e_{\mathrm{IS}}$ follows a Gaussian distribution:

$$\Omega(e_{\mathrm{IS}})\,\mathrm{d}e_{\mathrm{IS}} = \frac{e^{\alpha N}}{\sqrt{2\pi\sigma^2}} \exp\left[-\frac{(e_{\mathrm{IS}} - E_0)^2}{2\sigma^2}\right] \mathrm{d}e_{\mathrm{IS}}, \qquad [1]$$

where $e^{\alpha N}$ is the total number of basins in the PEL, E_0 is the most probable IS energy, and σ^2 is the variance of the distribution. Thus, three volume-dependent parameters $\{E_0, \sigma^2, \alpha\}$ are sufficient to characterize the distribution of basin depths at fixed volume, V.

To completely quantify the landscape, one also needs information on the basin shape, or equivalently, on the vibrational free energy when the system is constrained to a specific basin with IS energy e_{IS}. The corresponding basin's free energy,

$$F_{\mathcal{B}}(e_{\mathrm{IS}}, V, T) = e_{\mathrm{IS}} + f_{\mathrm{vib}}(e_{\mathrm{IS}}, V, T), \qquad [2]$$

accounts for vibrational motion within the PEL basins with energy e_{IS}. Here, $f_{\mathrm{vib}}(e_{\mathrm{IS}}, V, T)$ represents the average contribution to the Helmholtz free energy due to system exploring basins of the PEL with energy e_{IS}. The vibrational free energy, f_{vib}, can be decomposed into harmonic and anharmonic contributions:

$$f_{\mathrm{vib}}(e_{\mathrm{IS}}, V, T) = f_{\mathrm{harm}}(e_{\mathrm{IS}}, V, T) + f_{\mathrm{anharm}}(V, T), \qquad [3]$$

where $f_{\mathrm{anharm}}(V, T)$ is assumed to be e_{IS} independent. Within the harmonic approximation,

$$f_{\mathrm{harm}}(e_{\mathrm{IS}}, V, T) = k_{\mathrm{B}}T \left\langle \sum_{i=1}^{d-3} \ln\left(\frac{\hbar\omega_i}{k_B T}\right) \right\rangle_{e_{\mathrm{IS}}}. \qquad [4]$$

Here, k_{B} is the Boltzmann constant, $\{\omega_i\}$ are the normal mode frequencies of the system at a given IS, $\hbar$ is the reduced Planck constant, and the angle brackets denote an average over all ISs with energy e_{IS}. The logarithmic sum of the normal mode frequencies defines the shape function, $\mathcal{S}$, as

$$\mathcal{S}(e_{\mathrm{IS}}, V) \equiv \left\langle \sum_{i=1}^{d-3} \ln\left(\frac{\hbar\omega_i}{A_0}\right) \right\rangle_{e_{\mathrm{IS}}}, \qquad [5]$$

with $A_0 = 1$ kJ/mol as a reference scale. The shape function captures how basin vibrational properties vary systematically with depth. As commonly employed in previous computational studies (57, 58, 64), we find that the shape function is linear in e_{IS},

$$\mathcal{S}(e_{\mathrm{IS}}, V) = a(V) + b(V)e_{\mathrm{IS}}. \qquad [6]$$

In practice, extracting the linear relationship in Eq. **6** from numerical data requires statistical averaging, as MD simulations produce individual ISs with a continuous distribution of energies rather than multiple structures at identical energies. We employ an energy-based binned averaging protocol to establish the empirical relationship $\mathcal{S} = a + b\bar{e}_{\mathrm{IS}}$, where $\bar{e}_{\mathrm{IS}}$ represents statistically averaged IS energies. Different methods to compute $\bar{e}_{\mathrm{IS}}$ are discussed in *SI Appendix*, section 5.

Anharmonicity can be captured by fitting the anharmonic contribution to the potential energy as (59),

$$U_{\mathrm{anharm}}(V, T) = c_2(V)T^2 + c_3(V)T^3, \qquad [7]$$

from which the corresponding anharmonic contributions to the Helmholtz free energy and entropy follow.

Altogether, five parameters (seven if anharmonic contributions are included) fully determine all the thermodynamics of the system. $E_0(V)$ represents the typical energy scale of the liquid, $\sigma^2(V)$ quantifies the energetic heterogeneity, $\alpha(V)$ measures the configurational degeneracy, $a(V)$ and $b(V)$ capture how vibrational properties change with basin depth, while $c_2(V)$ and $c_3(V)$ quantify the anharmonicities of the PEL basins. Table 1 summarizes the seven parameters.

The Gaussian approximation of the PEL formalism, supplemented by the e_{IS}-dependence of the basin free energy, Eqs. **4** and **5**, enables analytical derivation of thermodynamic properties. For example, the average IS energy sampled by the system in equilibrium is given by

$$E_{\mathrm{IS}}(T) = E_0 - b\sigma^2 - \beta\sigma^2, \qquad [8]$$

Table 1. Key parameters in the potential energy landscape formalism and their physical significance

Parameter	Symbol	Physical meaning
Inherent structure energy	e_{IS}	Energy of a local minimum (basin bottom)
Mean IS energy	E_{IS}	Average basin depth sampled at temperature, T
Most probable IS energy	$E_0(V)$	Center of the Gaussian distribution of IS energies
Landscape variance	$\sigma^2(V)$	Width of the IS energy distribution
Basin degeneracy	$e^{\alpha(V)N}$	Total number of distinct basins
Shape function intercept	$a(V)$	Baseline vibrational entropy
Shape function slope	$b(V)$	How vibrational properties change with basin depth
Anharmonic coefficients	$c_2(V), c_3(V)$	Deviations from harmonic vibrations

which predicts a linear-dependence on $1/T$ with slope set by σ^2 and intercept by $E_0 - b\sigma^2$. Similarly, the configurational entropy follows as

$$\frac{S_{conf}}{k_B} = \alpha N - \tfrac{1}{2}\sigma^2(b+\beta)^2, \qquad [9]$$

where the first term reflects the basin multiplicity and the second encodes thermal sampling. In practice, $E_{IS}(T)$ and $\mathcal{S}(e_{IS})$ provide direct simulation routes to extract these parameters. A detailed treatment of the theoretical framework is provided in *SI Appendix*, section 2.

Inherent Structure Energy and the Gaussian Approximation. Fig. 2*A* shows how the average IS energy, E_{IS}, varies with density at different temperatures. The behavior is complex and temperature-dependent, encoding the structural transitions that underlie water's anomalies. At low temperatures (200 to 240 K), E_{IS} exhibits negative curvature with respect to density. Initially, E_{IS} increases with density, reaches a maximum near $\rho \approx 1.1$ g/cm^3, then decreases at higher densities. This unusual behavior reflects the competition between hydrogen-bond network optimization and geometric frustration (2, 55, 58, 66, 67).

At these low temperatures, water molecules at ice-like densities have sufficient space to form nearly ideal tetrahedral networks, accessing deep potential energy basins. As density increases toward 1.1 g/cm^3, geometric constraints begin to distort these networks, raising the typical IS energy. However, further compression beyond this point forces a structural transformation: the system abandons the open tetrahedral structure in favor of more compact arrangements with interpenetrating hydrogen-bond networks, accessing lower energy configurations despite the higher density (57, 66). The negative curvature of the IS energy versus density indicates the onset of an energetically unstable contribution to the free energy (66). At high temperatures (280 to 300 K), the curvature inverts, E_{IS} now decreases with initial compression before rising at the highest densities. The crossover temperature near 260 K marks the transition to a low-temperature regime in which the driving force for forming a low-density, hydrogen-bonded network becomes increasingly significant.

Fig. 2*B* provides a stringent test of the Gaussian approximation for the PEL (Eq. **8**). The excellent linearity of E_{IS} versus T^{-1} at $T \leq 280$ K, for all densities studied, validates the Gaussian approximation for the PEL of DP_MBpol water. This represents a nontrivial result. The DP model produces a PEL with Gaussian statistics, the same statistics observed in many simple liquids, empirical classical water models, and now quantum-accurate many-body representations. From the slopes of these linear fits, we extract σ^2 for each density. An alternative estimate of σ^2 can be obtained directly from the distributions of the $e_{IS}(T)$. *SI Appendix*, Fig. S10 compares the two methods and demonstrates that while individual temperature-based estimates of σ^2 exhibit considerable statistical scatter due to the finite number of configurations (~100 IS per temperature), their mean converges to the value calculated from the slopes. This variance quantifies the heterogeneity of the energy landscape, as larger values indicate a broader distribution of accessible basin depths (68).

The volume dependence of the variance of inherent structure energies, $\sigma^2(V)$, plays a central role in water's thermodynamic anomalies. Within the Gaussian PEL formalism, the condition

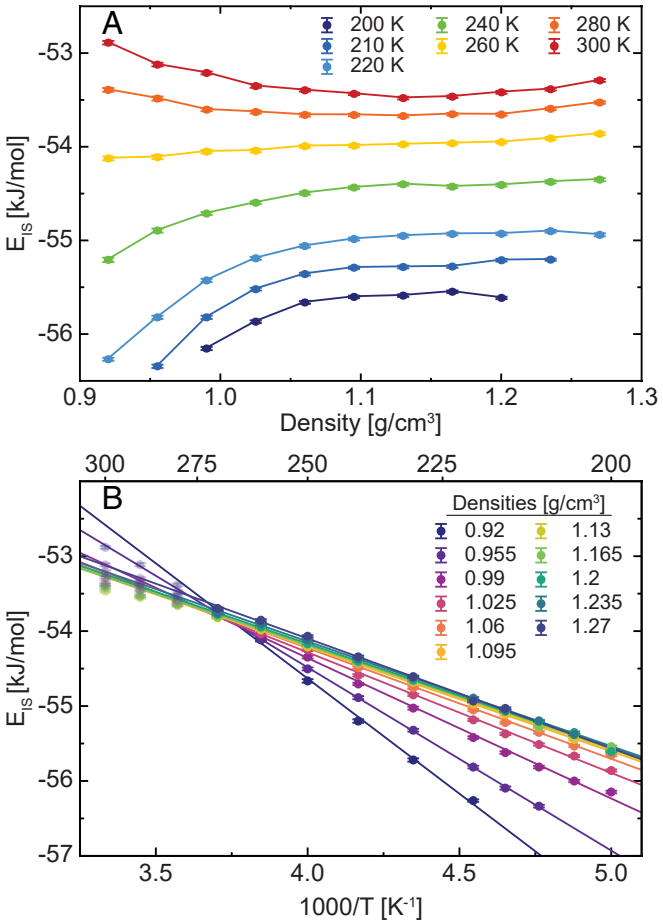

Fig. 2. Inherent structure energies as a function of density and temperature. (*A*) Inherent structure energy E_{IS} versus density at selected temperatures from 200 to 300 K. (*B*) The same data plotted as E_{IS} versus inverse temperature (1,000/T) showing the temperature-dependence at various densities ranging from 0.92 to 1.27 g/cm^3. The linear fits are performed over data at $T \leq 280$ K. The *Top* axis labels correspond to the temperature, T in K. Each data point represents an average over 100 independent inherent structures at each state point, with error bars indicating the SE of the mean.

$d\sigma^2/dV > 0$ is both necessary and sufficient for the existence of a density maximum (69). As shown in *SI Appendix*, Fig. S8, σ^2 exhibits a minimum near $\rho \approx 1.15$ g/cm^3. This same landscape feature also underlies the emergence of the LLCP at low temperatures. At sufficiently low temperature, isochores on the low–density side of the minimum exhibit anomalous behavior, with pressure increasing upon cooling, while those on the high–density side behave normally. This opposing behavior produces nonmonotonic pressure–volume isotherms, signaling mechanical instability and phase separation between LDL and HDL phases (69). Thus, within the PEL framework, both water's density anomaly and the liquid–liquid transition share a common microscopic origin. While the nonmonotonic density dependence of E_{IS} at low temperatures (Fig. 2*A*) provides valuable physical insight into the structural competition between tetrahedral and interpenetrating hydrogen-bond networks, the minimum in $\sigma^2(V)$ is the landscape feature responsible for these thermodynamic phenomena.

Basin Properties and Anharmonic Contributions. Fig. 3 demonstrates that the DP_MBpol shape function is linear in e_{IS}, as described by Eq. **6**. The linear relationship holds across all densities studied, with the intercept a and slope b providing the final parameters needed to fully characterize the Gaussian PEL of water.

While the PEL formalism with the Gaussian and harmonic approximations provides a theoretical foundation to describe liquids in general, water may exhibit anharmonicity. Fig. 4 tests the harmonic approximation for DP_MBpol water by plotting $\Delta U = U - E_{IS}$ versus temperature across all studied densities, where U is the potential energy of the system. The dashed line represents the theoretical harmonic prediction, $U_{harm} = 9Nk_BT/2$, while circles show the observed values from DP_MBpol simulations.

Fig. 4 reveals detectable anharmonicity in DP_MBpol water, as the observed energy exceeds the harmonic prediction at all state points. The anharmonic contribution amounts to about 6% of the vibrational potential energy at 200 K and increases to 16% at 300 K. These deviations exhibit modest density- and temperature-dependence, indicating that anharmonic contributions are both significant and physically meaningful. To capture these anharmonic effects, we employ the polynomial expansion in temperature from Eq. **7**. The fitted coefficients c_2 and c_3 (*SI Appendix*, Fig. S8) closely match, for all densities, those of the empirical q-TIP4P/F water model, (59) despite the fundamentally different origins of these potentials. What is striking is that this similarity persists even though previous studies employed pair-additive models, while DP_MBpol introduces a neural-network many-body representation. One might expect the increased complexity of the molecular interaction to substantially reshape the energy landscape, particularly its curvature, yet the statistics remain essentially unchanged. This robustness highlights not only that certain landscape properties are insensitive to the details of the interaction potential, but also that some empirical water models capture the essential physics of water with remarkable accuracy.

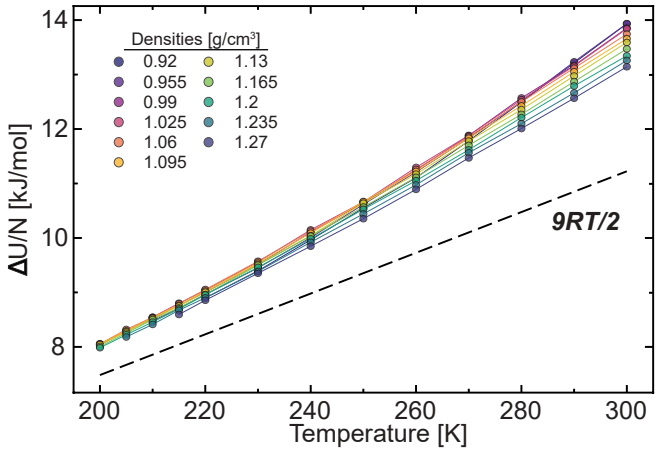

Fig. 4. Anharmonic analysis of the potential energy landscape: a test of the harmonic approximation. Circles show $\Delta U = U - E_{IS}$ for densities spanning from 0.92 to 1.27 g/cm^3, while the dashed line indicates the theoretical harmonic energy for a flexible water molecule ($U_{harm} = 9RT/2$, [R is the gas constant]). Deviations from this line represent the anharmonic contributions to the total energy U.

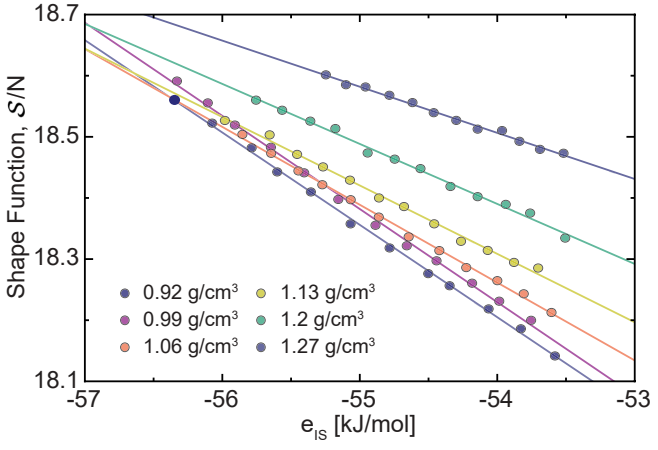

Fig. 3. Basin shape function $\mathcal{S}$ versus inherent structure energy for selected densities. Within the harmonic approximation, $\mathcal{S}(e_{IS})$ quantifies the average curvature of the PEL basins with IS energy e_{IS}. The solid lines correspond to linear fits according to Eq. **6**, from which the PEL parameters a and b are extracted.

Configurational Entropy. Complete characterization of water using the PEL formalism requires absolute free energies to calculate the configurational entropy (70). Obtaining these free energies for the DP_MBpol model presents a unique challenge related to both the power and limitations of MLPs and their training data. Because DP_MBpol was trained exclusively on condensed phase configurations (liquid water and ice polymorphs), it cannot reliably represent the very low density and high temperature vapor phase. In practice, simulations of the vapor phase in the ideal-gas limit with DP_MBpol resulted in unphysically small distances between O and H atoms. This training limitation precludes the standard approach of connecting directly to an ideal gas reference state.

To circumvent this challenge, we employed a multistage TI strategy, schematically illustrated in Fig. 1. We begin with an ideal gas of $N = 512$ MB-pol molecules at $T = 700$ K (above the MB-pol critical temperature to avoid crossing a first-order phase transition along the TI path) and a large volume where intermolecular interactions are negligible. From this well-defined reference state, we performed an isothermal compression of MB-pol to reach a target condensed phase density ($T = 700$ K, $\rho \approx 0.92$ g/cm^3). We then interconvert from MB-pol to DP_MBpol using an overlapping distribution method (71), in which we computed the free energy difference between the two

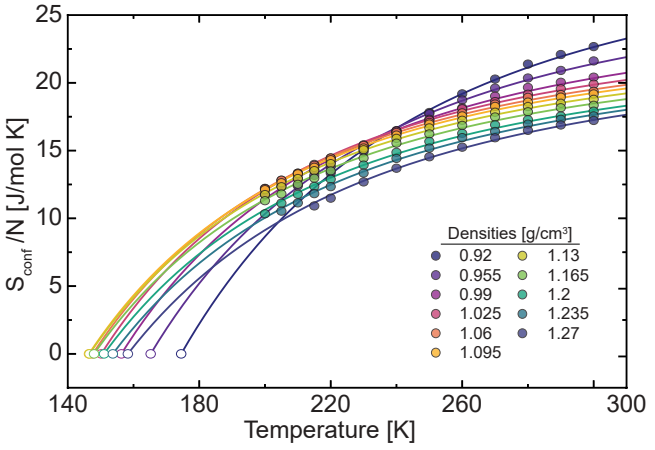

Fig. 5. Configurational entropy S_{conf} versus temperature for different densities. The solid circles are the values of S_{conf} obtained numerically by TI and the lines are the corresponding fits using Eq. **9**, where only α is used as a fitting parameter. The white circles indicate the Kauzmann temperature, $T_{\text{K}}(V)$, obtained by extrapolation of the solid lines to $S_{\text{conf}} = 0$.

models by sampling their energy distributions over the same set of configurations. We performed this interconversion at $T = 700$ K and $\rho \approx 0.92$ g/cm^3, where both models are stable, giving a free energy difference between models of $\Delta F/N = 0.0137\, k_{\text{B}}T$. Finally, isochoric cooling brings the system to the temperatures of interest. Technical details are provided in *SI Appendix*, section 3.

Fig. 5 shows the configurational entropy of DP_MBpol water calculated as the difference between the liquid and vibrational entropies (*SI Appendix*, Fig. S3). The solid lines in Fig. 5 show the theoretical prediction according to Eq. **9**, where only α is a fitting parameter. The extrapolation to $S_{\text{conf}} = 0$ defines the Kauzmann temperature, T_K. The extrapolation to $S_{\text{conf}} = 0$ in Fig. 5 defines T_K within the Gaussian approximation of the PEL. However, deviations from Gaussian statistics at low temperatures (or low IS energies) could change our estimated values for T_{K}.

Equation of State and Liquid–Liquid Critical Point. The power of the PEL approach lies in its ability to provide an analytical EoS. We can derive the pressure EoS from the free energy as a function of temperature and volume:

$$P = -\left(\frac{\partial F}{\partial V}\right)_T = \sum_{i=-1}^{3} P_i(V)T^i, \qquad [10]$$

where the coefficients $P_i(V)$ depend on volume derivatives of the landscape parameters (*SI Appendix*, section 2).

Fig. 6*A* demonstrates that the PEL-based EoS accurately reproduces the MD simulation data across all temperatures and densities studied. While we expected the EoS to provide a good description of the MD data at low temperatures, it fits the entire dataset remarkably well. This success gives confidence in extrapolating to lower temperatures where direct simulation becomes prohibitive.

The pressure–volume diagram (Fig. 6*B*) reveals the signature of a first-order liquid–liquid phase transition (LLPT) through the emergence of van der Waals loops. At high temperatures (red lines), the P-V isotherms show thermodynamically stable monotonic behavior, where decompression leads to a smooth, continuous decrease in pressure as expected for a single-phase liquid. However, as temperature decreases (progressing toward blue lines), the isotherms develop nonmonotonic character. Regions emerge where $(\partial P/\partial V)_T > 0$, that is, pressure increases with expanding volume. This behavior violates thermodynamic stability, which requires $(\partial P/\partial V)_T \leq 0$ for any stable/metastable phase. Such instability signals that the homogeneous liquid has become mechanically unstable and must spontaneously separate into two coexisting phases with different densities.

The limits of stability for the two liquid phases (low-density and high-density liquids, LDL and HDL) are given by the spinodal curves (purple lines in Fig. 6*B*), obtained from the condition $(\partial P/\partial V)_T = 0$. The binodal curves (black lines in Fig. 6 *B* and *C*) define the true coexistence region and are constructed using the Maxwell equal-area rule. This construction ensures that the chemical potentials of the coexisting LDL and HDL phases are equal at a given temperature and pressure. Between the spinodal and binodal curves lies the metastable region, where the LDL and HDL can persist as a metastable homogeneous phase. As the temperature increases toward the critical point, the van der Waals loops progressively shrink, and the distinction between the LDL and HDL phases diminishes. The spinodal curves converge, the metastable region narrows, and the density difference between coexisting phases decreases. At the critical temperature, the van der Waals loop vanishes entirely. The inflection point where $(\partial P/\partial V)_T = 0$ and $(\partial^2 P/\partial V^2)_T = 0$ defines the location of the liquid–liquid critical point (LLCP) to be $T_c \approx 190$ K, $P_c \approx 1{,}043$ bar, and $\rho_c \approx 0.97$ g/cm^3. The location of the LLCP shows excellent agreement with the recently published values for this model estimated from extensive MD simulations: $T_c = 193 \pm 5$ K and $P_c = 1{,}050 \pm 50$ bar (47). Above this temperature, no amount of pressure can induce liquid–liquid phase separation, the system exhibits only continuous crossover behavior between LDL-like and HDL-like regions, marked by the Widom line (defined as the maximum in the compressibility).

Fig. 6*C* presents the complete phase diagram in the temperature-density plane, including the Kauzmann temperature line, T_{K}. On the low-density side, T_K is higher relative to the high-density side, reflecting the slower dynamics characteristic of the open, tetrahedral network compared to the high-density liquid. In HDL, interstitial molecules—fifth neighbors that penetrate between the first and second coordination shells—act as catalytic defect sites that facilitate network reorganization, reducing activation barriers for molecular motion (72–74). The Kauzmann temperature of the LDL at 1 bar ($T_{\text{K}} \approx 157$ K) is also substantially higher than the calorimetric glass-transition values observed experimentally, ($T_{\text{g}} = 136$ K) (75). This overestimation has often been attributed to the breakdown of the Gaussian approximation as e_{IS} approaches the lowest IS energy of the liquid/glass available in the PEL (76). However, despite the disparity in experimental and computational timescales, it is noteworthy that the simulated glass-transition temperatures obtained with DP_MBpol are also higher than experimental values (48). Thus, despite the overall accuracy of MBpol-based models, achieving more reliable values of both T_{K} and T_{g} remains an outstanding challenge in water modeling.

The existence of the LLCP emerges naturally from the nonmonotonic density dependence of σ^2 (56), the same property that produces the density maximum at higher temperatures. This unified explanation of water's anomalies, from the density maximum to the liquid–liquid transition, demonstrates the power of the PEL framework in connecting microscopic landscape features to macroscopic thermodynamic behavior. The

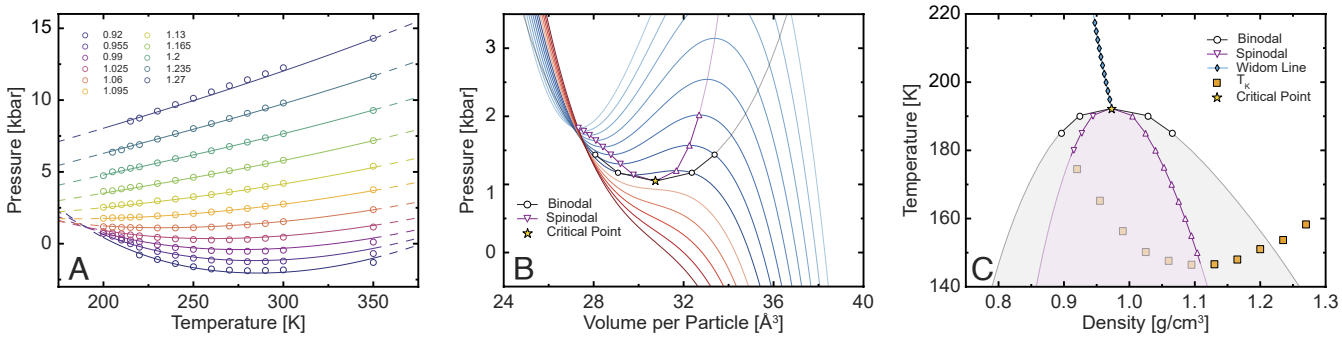

Fig. 6. Phase behavior calculated from the PEL equation of state. (*A*) Pressure–temperature phase diagram. Circles show MD simulation data while lines represent the PEL equation of state predictions. (*B*) Pressure–volume phase diagram revealing van der Waals loops characteristic of a first-order phase transition. Spinodal curves (purple) represent stability limits while binodal curves (black) calculated from a Maxwell equal-area construction define coexistence. Isotherms are shown for temperatures from 150 K to 215 K in 5 K increments, from blue to red. (*C*) Temperature-density phase diagram showing the liquid–liquid critical point at $T_c \approx 190$ K, the Widom line (blue) extending into the one-phase region, and Kauzmann temperatures (orange). The coexistence region [gray shading (metastable); purple shading (unstable)] separates low-density (LDL) and high-density (HDL) liquid phases.

quantitative agreement with experimental estimates (5) and other theoretical predictions (47) validates both our analysis based on the PEL approach and the accuracy of the DP_MBpol neural network potential in capturing water's essential physics.

Discussion

This work establishes that machine-learned potentials preserve the landscape statistics governing liquid behavior, opening opportunities for studying water and other complex fluids at previously inaccessible levels of accuracy and scale. By demonstrating that the DP_MBpol model reproduces the Gaussian PEL topology, exhibits the correct density-dependence of the PEL parameters for anomalous behavior, and predicts a LLCP consistent with previous estimates, we validate both the fidelity of machine learning approaches and the Gaussian PEL formalism even when many-body correlations of quantum origin are explicitly included, as in the MBpol model.

The PEL parameters we extract for in this work are qualitatively similar to those from previous studies of empirical water models, including SPC/E, TIP4P/2005, and q-TIP4P/F. This suggests that the key features of water's energy landscape, the Gaussian distribution of basin depths and the nonmonotonic density dependence of σ^2, are robust to the details of the interaction potential and appear to be generic features of accurate water models. The quantum-mechanical information (and many-body interactions) embedded in DP_MBpol does not fundamentally alter the PEL but provides quantitatively accurate energetics and many-body effects essential for more quantitative reproduction of experimental observables. This validates the physical picture that water's anomalies arise from landscape features captured even by simple models, while quantitative predictive accuracy requires the detailed energetics that quantum-trained potentials provide.

Several limitations of this study point toward exciting future directions. We restricted the current analysis to classical nuclei. Incorporating nuclear quantum effects through path integral methods could reveal how zero-point motion and tunneling modify the PEL topology, particularly near the LLCP where quantum fluctuations may play a decisive role (62, 63). Additionally, extensions of the PEL formalism with DP_MBpol/MLPs simulations to aqueous solutions where solutes can dramatically alter the energy landscape would provide insights into biological and atmospheric processes.

Given the recent discovery of medium density amorphous ice (77) and the role of shear-driven processes in amorphous ice formation (78), an exciting further direction would be to incorporate shear as an additional variable in the PEL framework. In equilibrium, the potential energy landscape is independent of shear; however, shear can drive the system to explore different regions of this landscape, altering the statistics of basin occupation and transition pathways (79). In situations where shear arises from confinement or externally imposed strain, such that additional boundary or deformation potentials contribute to the energy of the system, the effective landscape can be modified. Developing a generalized PEL framework that accounts for how mechanical driving changes landscape exploration, and in some cases the effective landscape itself, could reveal how shear influences the low temperature behavior and glass formation in water.

Finally, with increasing computational resources, it may soon be possible to investigate the low-density, low-temperature state points numerically, potentially revealing the breakdown of the Gaussian landscape approximation. Recent work (80) suggests that optimally sized systems can access lower temperatures where non-Gaussian landscape features may become physically relevant. For water, determining the characteristic system size beyond which finite-size effects vanish, which may differ among water models, could enable more efficient exploration of the deep supercooled regime where the Gaussian approximation is expected to fail, potentially providing more reliable estimates of both T_g and T_K. Despite the success of MBpol-based models, current simulations predict values that are systematically higher than experiment, highlighting a key open challenge in water modeling.

The success of our PEL analysis for this MLP suggests that researchers could apply similar approaches to other machine-learned Hamiltonians, where the connection between local interactions and emergent behavior remains poorly understood. As machine learning models become increasingly sophisticated and approach chemical accuracy within computationally tractable efficiency, the combination of MLPs and statistical mechanical frameworks like PEL theory promises to advance our understanding of complex molecular systems substantially.

Materials and Methods

Molecular Dynamics Simulations. Molecular dynamics simulations were carried out with the LAMMPS simulation software, version 2 August 2023 (81) patched with the DPMD-kit, version 3.0.1 (40, 41). Periodic boundary conditions were applied in all three dimensions. Water was modeled

with a Deep Potential model previously trained on MB-pol reference data (39). The equations of motion were integrated using the velocity–Verlet algorithm with a time step of 0.5 fs. All simulations were performed in the canonical (NVT) ensemble, and the temperature was controlled by a Nosé–Hoover thermostat set to the target production temperature with a damping parameter of 0.5 ps. Thermodynamic properties were saved every 5,000 steps, while atomic configurations were recorded every 25,000 steps for trajectory analysis.

Eleven different densities from 0.92 to 1.27 g/cm^3 and thirteen different temperatures between 200 and 300 K were investigated (Fig. 1). The duration of each trajectory was determined by monitoring the mean square displacement (MSD) of the water molecules. We define the structural relaxation time, τ, as the time required for the MSD of the system to reach 1 nm^2. We required that both the equilibration and production segments of each simulation exceeded τ, ensuring that each trajectory sampled beyond the intrinsic relaxation dynamics of the liquid. This procedure guaranteed that the simulations captured both equilibrium and dynamical properties reliably. The values of τ, together with the total simulation lengths corresponding to each state point, are reported in *SI Appendix*, section 1.

Inherent Structure and Normal Mode Analysis. Inherent structures were obtained by energy minimization of configurations sampled from equilibrium NVT trajectories. From each trajectory, 100 equally spaced configurations were selected and minimized using the conjugate gradient method as implemented in LAMMPS with the DP_MBpol model. Energy minimization proceeded until convergence was achieved, defined as an energy change below 10^{-4} eV/atom and a maximum atomic force below 10^{-6} eV/Å.

We then calculated the Hessian for 25 IS, chosen at equal intervals along the trajectories. The mass-weighted Hessian was computed using the LAMMPS PHONON package, which evaluates the second derivatives of the potential energy with respect to atomic displacements via finite-difference perturbations. The resulting Hessian matrices were diagonalized using the LAPACK routine SSYEV, which computes the eigenvalues of real symmetric matrices. From the full set of frequencies, the vibrational density of states was obtained (*SI Appendix*, section 5).

Free Energy Calculations. We calculated free energies for the DP_MBpol model following a multistep thermodynamic integration procedure (Fig. 1). We begin with the calculation of the partition function of an ideal gas of $N = 512$ MB-pol water molecules at $T = 700$ K and very low density, where the ideal gas approximation is accurate.

The total partition function of an ideal gas of N molecules at temperature T is

$$Z_{ig} = \frac{(Z_{\text{mol}}V)^N}{N!\lambda^{3N}}, \quad [11]$$

where λ is the center of mass thermal de Broglie wavelength. Because the DP model was not trained on the gas phase and can exhibit nonphysical behavior at low density and high temperature (nonphysical small distances between O and H atoms), the reference ideal-gas free energy was computed using the MB-pol model, which is well behaved in this regime.

From this reference state (black star in Fig. 1), a thermodynamic integration was performed along the $T = 700$ K isotherm to compress the system from the ideal gas volume to a target, condensed-phase density. The excess free energy was obtained via integration of the pressure EoS:

$$\Delta F_{\text{ex}} = N\int_{\rho_{\text{start}}}^{\rho_{\text{final}}} \frac{P_{\text{ex}}(\rho)}{\rho^2}\, d\rho \quad [12]$$

with the excess pressure represented as a polynomial expansion in the density. In the above equation, the subscript "ex" denotes excess over the corresponding ideal gas property at the given density and temperature (e.g., $P_{\text{ex}} = P - \rho k_B T$)

At the target thermodynamic state point, (T =700 K, $\rho = 0.92$ g/cm^3), the MB-pol and DP_MBpol models were connected through the overlapping distribution method of Bennett (71), which relates the free energy difference between models to the shift required to collapse probability distributions of the energy difference $\Delta U = U_{\text{DP\_MBpol}} - U_{\text{MB-pol}}$.

Finally, the free energy of the DP_MBpol model was propagated from $T =$ 700 K to the target temperature via isochoric thermodynamic integration:

$$S(T) = S(T_0) + \int_{T_0}^{T} \frac{1}{T'}\frac{\partial U}{\partial T'} dT', \quad [13]$$

where $U(T)$ is the internal energy obtained from simulation data. This procedure gave the free energy of the DP_MBpol model at each state point. Complete derivation of the equations, implementation details, and supporting analysis are provided in *SI Appendix*, section 3.

Data, Materials, and Software Availability. Code/SimulationResults data have been deposited in Data From: "Energy Landscape Statistics and Thermodynamics of a Machine-Learned Model of Water" (https://doi.org/10.34770/2nkt-5c07) (82).

ACKNOWLEDGMENTS. R.J.S., A.G., and P.G.D. acknowledge support from the "Chemistry in Solution and at Interfaces" Center funded by the U.S. Department of Energy through Award No. DE-SC0019394. N.G. is thankful to the NSF (grant number CHE-2223461), and to the NSF-CREST Center for Interface Design and Engineered Assembly of Low Dimensional systems (IDEALS; grant numbers HRD-1547380 and HRD-2112550). F.S. acknowledges support from MIUR-PRIN 2022JWAF7Y, Cineca Italian Super Computing Resource Allocation initiative and ICSC-Centro Nazionale di Ricerca in High Performance Computing, Big Data and Quantum Computing, funded by the European Union "NextGenerationEU". Simulations and analyses were performed using resources from Princeton Research Computing at Princeton University, which is a consortium led by the Princeton Institute for Computational Science and Engineering and Office of Information Technology's Research Computing.

Author affiliations: [a]Department of Chemistry, Princeton University, Princeton, NJ 08544; [b]Dipartimento di Fisica, Sapienza Università di Roma, Roma 00185, Italy; [c]Department of Physics, Brooklyn College of the City University of New York, Brooklyn, NY 11210; [d]Ph.D. Programs in Physics and Chemistry, The Graduate Center of the City University of New York, New York, NY 10016; and [e]Department of Chemical and Biological Engineering, Princeton University, Princeton, NJ 08544

1. R. Speedy, C. Angell, Isothermal compressibility of supercooled water and evidence for a thermodynamic singularity at −45 C. *J. Chem. Phys.* **65**, 851–858 (1976).
2. P. H. Poole, F. Sciortino, U. Essmann, H. E. Stanley, Phase behaviour of metastable water. *Nature* **360**, 324–328 (1992).
3. P. G. Debenedetti, Supercooled and glassy water. *J. Phys. Condens. Matter* **15**, R1669 (2003).
4. P. Gallo *et al.*, Water: A tale of two liquids. *Chem. Rev.* **116**, 7463–7500 (2016).
5. K. H. Kim *et al.*, Maxima in the thermodynamic response and correlation functions of deeply supercooled water. *Science* **358**, 1589–1593 (2017).
6. J. C. Palmer, P. H. Poole, F. Sciortino, P. G. Debenedetti, Advances in computational studies of the liquid-liquid transition in water and water-like models. *Chem. Rev.* **118**, 9129–9151 (2018).
7. D. Eisenberg, W. Kauzmann, *The Structure and Properties of Water* (Oxford University Press, 2005).
8. E. Brini *et al.*, How water's properties are encoded in its molecular structure and energies. *Chem. Rev.* **117**, 12385–12414 (2017).
9. W. L. Jorgensen, J. Chandrasekhar, J. D. Madura, R. W. Impey, M. L. Klein, Comparison of simple potential functions for simulating liquid water. *J. Chem. Phys.* **79**, 926–935 (1983).
10. H. J. Berendsen, J. R. Grigera, T. P. Straatsma, The missing term in effective pair potentials. *J. Phys. Chem.* **91**, 6269–6271 (1987).
11. G. A. Cisneros *et al.*, Modeling molecular interactions in water: From pairwise to many-body potential energy functions. *Chem. Rev.* **116**, 7501–7528 (2016).
12. S. P. Kadaoluwa Pathirannahalage *et al.*, Systematic comparison of the structural and dynamic properties of commonly used water models for molecular dynamics simulations. *J. Chem. Inf. Model.* **61**, 4521–4536 (2021).
13. J. L. Abascal, C. Vega, A general purpose model for the condensed phases of water: TIP4P/2005. *J. Chem. Phys.* **123**, 234505 (2005).
14. J. Abascal, E. Sanz, R. García Fernández, C. Vega, A potential model for the study of ices and amorphous water: TIP4P/Ice. *J. Chem. Phys.* **122**, 234511 (2005).
15. C. Vega, E. Sanz, J. Abascal, E. Noya, Determination of phase diagrams via computer simulation: Methodology and applications to water, electrolytes and proteins. *J. Phys. Condens. Matter* **20**, 153101 (2008).
16. J. L. Abascal, C. Vega, Widom line and the liquid-liquid critical point for the TIP4P/2005 water model. *J. Chem. Phys.* **133**, 234502 (2010).

17. T. Hasegawa, Y. Tanimura, A polarizable water model for intramolecular and intermolecular vibrational spectroscopies. *J. Phys. Chem. B* **115**, 5545–5553 (2011).
18. L. P. Wang *et al*., Systematic improvement of a classical molecular model of water. *J. Phys. Chem. B* **117**, 9956–9972 (2013).
19. D. J. Arismendi-Arrieta, M. Riera, P. Bajaj, R. Prosmiti, F. Paesani, I-TTM model for ab initio-based ion-water interaction potentials. 1. Halide-water potential energy functions. *J. Phys. Chem. B* **120**, 1822–1832 (2016).
20. H. Jiang, O. A. Moultos, I. G. Economou, A. Z. Panagiotopoulos, Hydrogen-bonding polarizable intermolecular potential model for water. *J. Phys. Chem. B* **120**, 12358–12370 (2016).
21. R. Car, M. Parrinello, Unified approach for molecular dynamics and density-functional theory. *Phys. Rev. Lett.* **55**, 2471 (1985).
22. B. Santra, A. Michaelides, M. Scheffler, On the accuracy of density-functional theory exchange-correlation functionals for H bonds in small water clusters: Benchmarks approaching the complete basis set limit. *J. Chem. Phys.* **127**, 184104 (2007).
23. M. D. Baer *et al*., Re-examining the properties of the aqueous vapor-liquid interface using dispersion corrected density functional theory. *J. Chem. Phys.* **135**, 124712 (2011).
24. P. Montero, C. de Hijes Dellago, R. Jinnouchi, G. Kresse, Density isobar of water and melting temperature of ice: Assessing common density functionals. *J. Chem. Phys.* **161**, 131102 (2024).
25. J. Behler, M. Parrinello, Generalized neural-network representation of high-dimensional potential-energy surfaces. *Phys. Rev. Lett.* **98**, 146401 (2007).
26. P. Friederich, F. Häse, J. Proppe, A. Aspuru-Guzik, Machine-learned potentials for next-generation matter simulations. *Nat. Mater.* **20**, 750–761 (2021).
27. E. Kocer, T. W. Ko, J. Behler, Neural network potentials: A concise overview of methods. *Annu. Rev. Phys. Chem.* **73**, 163–186 (2022).
28. I. Batatia, D. P. Kovacs, G. Simm, C. Ortner, G. Csányi, MACE: Higher order equivariant message passing neural networks for fast and accurate force fields. *Adv. Neural Inf. Process. Syst.* **35**, 11423–11436 (2022).
29. C. Zhang *et al*., Modeling liquid water by climbing up Jacob's ladder in density functional theory facilitated by using deep neural network potentials. *J. Phys. Chem. B* **125**, 11444–11456 (2021).
30. J. Daru, H. Forbert, J. Behler, D. Marx, Coupled cluster molecular dynamics of condensed phase systems enabled by machine learning potentials: Liquid water benchmark. *Phys. Rev. Lett.* **129**, 226001 (2022).
31. T. Maxson, T. Szilvási, Transferable water potentials using equivariant neural networks. *J. Phys. Chem. Lett.* **15**, 3740–3747 (2024).
32. A. Omranpour, P. Montero De Hijes, J. Behler, C. Dellago, Perspective: Atomistic simulations of water and aqueous systems with machine learning potentials. *J. Chem. Phys.* **160**, 170901 (2024).
33. P. Montero de Hijes, C. Dellago, R. Jinnouchi, B. Schmiedmayer, G. Kresse, Comparing machine learning potentials for water: Kernel-based regression and Behler-Parrinello neural networks. *J. Chem. Phys.* **160**, 114107 (2024).
34. K. Xu *et al*., NEP-MB-pol: A unified machine-learned framework for fast and accurate prediction of water's thermodynamic and transport properties. *NPJ Comput. Mat.* **11**, 279 (2025).
35. L. Zhang, H. Wang, R. Car, E. Weinan, Phase diagram of a deep potential water model. *Phys. Rev. Lett.* **126**, 236001 (2021).
36. T. E. Gartner III, P. M. Piaggi, R. Car, A. Z. Panagiotopoulos, P. G. Debenedetti, Liquid-liquid transition in water from first principles. *Phys. Rev. Lett.* **129**, 255702 (2022).
37. P. G. Debenedetti, F. Sciortino, G. H. Zerze, Second critical point in two realistic models of water. *Science* **369**, 289–292 (2020).
38. J. Weis, F. Sciortino, A. Z. Panagiotopoulos, P. G. Debenedetti, Liquid-liquid criticality in the WAIL water model. *J. Chem. Phys.* **157**, 024502 (2022).
39. S. L. Bore, F. Paesani, Realistic phase diagram of water from "first principles" data-driven quantum simulations. *Nat. Comm.* **14**, 3349 (2023).
40. L. Zhang, J. Han, H. Wang, R. Car, E. Weinan, Deep potential molecular dynamics: A scalable model with the accuracy of quantum mechanics. *Phys. Rev. Lett.* **120**, 143001 (2018).
41. H. Wang, L. Zhang, J. Han, E. Weinan, DeePMD-kit: A deep learning package for many-body potential energy representation and molecular dynamics. *Comput. Phys. Commun.* **228**, 178–184 (2018).
42. V. Babin, C. Leforestier, F. Paesani, Development of a "first principles" water potential with flexible monomers: Dimer potential energy surface, VRT spectrum, and second virial coefficient. *J. Chem. Theory Comput.* **9**, 5395–5403 (2013).
43. V. Babin, G. R. Medders, F. Paesani, Development of a "first principles" water potential with flexible monomers. II: Trimer potential energy surface, third virial coefficient, and small clusters. *J. Chem. Theory Comput.* **10**, 1599–1607 (2014).
44. G. R. Medders, V. Babin, F. Paesani, Development of a "first-principles" water potential with flexible monomers. III. Liquid phase properties. *J. Chem. Theory Comput.* **10**, 2906–2910 (2014).
45. T. E. Gartner III *et al*., Anomalies and local structure of liquid water from boiling to the supercooled regime as predicted by the many-body MB-pol model. *J. Phys. Chem. Lett.* **13**, 3652–3658 (2022).
46. E. Palos *et al*., Current status of the MB-pol data-driven many-body potential for predictive simulations of water across different phases. *J. Chem. Theory Comput.* **20**, 9269–9289 (2024).
47. F. Sciortino, Y. Zhai, S. Bore, F. Paesani, Constraints on the location of the liquid-liquid critical point in water. *Nat. Phys.* **21**, 1–6 (2025).
48. R. J. Szukalo, N. Giovambattista, P. G. Debenedetti, Computational investigation of water glasses using machine-learning potentials. *Proc. Natl. Acad. Sci. U.S.A.* **122**, e2509609122 (2025).
49. F. H. Stillinger, P. G. Debenedetti, Energy landscape diversity and supercooled liquid properties. *J. Chem. Phys.* **116**, 3353–3361 (2002).
50. M. Goldstein, Viscous liquids and the glass transition: A potential energy barrier picture. *J. Chem. Phys.* **51**, 3728–3739 (1969).
51. P. G. Debenedetti, F. H. Stillinger, Supercooled liquids and the glass transition. *Nature* **410**, 259–267 (2001).
52. D. Wales, *Energy Landscapes: Applications to Clusters, Biomolecules and Glasses* (Cambridge University Press, 2004).
53. F. Sciortino, Potential energy landscape description of supercooled liquids and glasses. *JSTAT* **2005**, P05015 (2005).
54. A. Heuer, Exploring the potential energy landscape of glass-forming systems: From inherent structures via metabasins to macroscopic transport. *J. Phys. Condens. Matter* **20**, 373101 (2008).
55. C. Roberts, P. Debenedetti, F. Stillinger, Equation of state of the energy landscape of SPC/E water. *J. Phys. Chem. B* **103**, 10258–10265 (1999).
56. E. La Nave, S. Mossa, F. Sciortino, Potential energy landscape equation of state. *Phys. Rev. Lett.* **88**, 225701 (2002).
57. P. H. Handle, F. Sciortino, Potential energy landscape of TIP4P/2005 water. *J. Chem. Phys.* **148**, 134505 (2018).
58. P. H. Handle, F. Sciortino, N. Giovambattista, Glass polymorphism in TIP4P/2005 water: A description based on the potential energy landscape formalism. *J. Chem. Phys.* **150**, 244506 (2019).
59. A. Eltareb, G. E. Lopez, N. Giovambattista, Potential energy landscape of a flexible water model: Equation of state, configurational entropy, and Adam-Gibbs relationship. *J. Chem. Phys.* **160**, 154510 (2024).
60. T. E. Markland *et al*., Quantum fluctuations can promote or inhibit glass formation. *Nat. Phys.* **7**, 134–137 (2011).
61. N. Giovambattista, G. E. Lopez, Potential energy landscape formalism for quantum liquids. *Phys. Rev. Res.* **2**, 043441 (2020).
62. A. Eltareb, G. E. Lopez, N. Giovambattista, Evidence of a liquid-liquid phase transition in h_2o and d_2o from path-integral molecular dynamics simulations. *Sci. Rep.* **12**, 6004 (2022).
63. Y. Zhou, G. E. Lopez, N. Giovambattista, The harmonic and gaussian approximations in the potential energy landscape formalism for quantum liquids. *J. Chem. Theory Comput.* **20**, 1847–1861 (2024).
64. A. Neophytou, F. Sciortino, Potential energy landscape of a coarse grained model for water: MI-bop. *J. Chem. Phys.* **160**, 114502 (2024).
65. A. Heuer, S. Büchner, Why is the density of inherent structures of a Lennard-Jones-type system gaussian? *J. Phys. Condens. Matter* **12**, 6535 (2000).
66. F. Sciortino, P. H. Poole, U. Essmann, H. Stanley, Line of compressibility maxima in the phase diagram of supercooled water. *Phys. Rev. E* **55**, 727 (1997).
67. J. Russo, F. Leoni, F. Martelli, F. Sciortino, The physics of empty liquids: From patchy particles to water. *Rep. Prog. Phys.* **85**, 016601 (2022).
68. S. Sastry, The relationship between fragility, configurational entropy and the potential energy landscape of glass-forming liquids. *Nature* **409**, 164–167 (2001).
69. F. Sciortino, E. La Nave, P. Tartaglia, Physics of the liquid-liquid critical point. *Phys. Rev. Lett.* **91**, 155701 (2003).
70. L. Berthier, M. Ozawa, C. Scalliet, Configurational entropy of glass-forming liquids. *J. Chem. Phys.* **150**, 160902 (2019).
71. D. Frenkel, B. Smit, *Understanding Molecular Simulation* (Academic Press Inc., USA, ed. 2, 2001).
72. F. Sciortino, A. Geiger, H. E. Stanley, Effect of defects on molecular mobility in liquid water. *Nature* **354**, 218–221 (1991).
73. P. H. Poole, S. R. Becker, F. Sciortino, F. W. Starr, Dynamical behavior near a liquid-liquid phase transition in simulations of supercooled water. *J. Phys. Chem. B* **115**, 14176–14183 (2011).
74. F. Martelli, Unravelling the contribution of local structures to the anomalies of water: The synergistic action of several factors. *J. Chem. Phys.* **150**, 094506 (2019).
75. G. Johari, A. Hallbrucker, E. Mayer, The glass-liquid transition of hyperquenched water. *Nature* **330**, 552–553 (1987).
76. A. Moreno *et al*., Non-gaussian energy landscape of a simple model for strong network-forming liquids: Accurate evaluation of the configurational entropy. *J. Chem. Phys.* **124**, 204509 (2006).
77. A. Rosu-Finsen *et al*., Medium-density amorphous ice. *Science* **379**, 474–478 (2023).
78. I. de Almeida Ribeiro *et al*., Medium-density amorphous ice unveils shear rate as a new dimension in water's phase diagram. *Proc. Natl. Acad. Sci. U.S.A.* **121**, e2414444121 (2024).
79. M. Blank-Burian, A. Heuer, Shearing small glass-forming systems: A potential energy landscape perspective. *Phys. Rev. E* **98**, 033002 (2018).
80. A. D. Parmar, A. Heuer, Depleting states dictate the ideal glass and physics of glass transition. arXiv [Preprint] (2023). http://arxiv.org/abs/2307.10143 (Accessed 21 January 2026).
81. A. P. Thompson *et al*., LAMMPS-a flexible simulation tool for particle-based materials modeling at the atomic, MESO, and continuum scales. *Comput. Phys. Commun.* **271**, 108171 (2022).
82. R. J. Szukalo *et al*., Data from "Energy landscape statistics and thermodynamics of a machine-learned model of water." Princeton Data Commons. https://doi.org/10.34770/2nkt-5c07. Deposited 16 February 2026.